



This open access document is published as a preprint in the Beilstein Archives with doi: 10.3762/bxiv.2019.16.v1 and is considered to be an early communication for feedback before peer review. Before citing this document, please check if a final, peer-reviewed version has been published in the Beilstein Journal of Nanotechnology.

This document is not formatted, has not undergone copyediting or typesetting, and may contain errors, unsubstantiated scientific claims or preliminary data.

**Preprint Title** Fabrication and characterization of  $\text{Si}_{1-x}\text{Ge}_x$  nanocrystals in as-grown and annealed structures: A comparative study

**Authors** Muhammad Taha Sultan, Valentin Serban Teodorescu, Jón Tómas Guðmundsson, Andrei Manolescu, Magdalena Lidia Ciurea and Halldór Guðfinnur Svavarsson

**Article Type** Full Research Paper

**ORCID® iDs** Muhammad Taha Sultan - <https://orcid.org/0000-0002-1167-3513>;  
Jón Tómas Guðmundsson - <https://orcid.org/0000-0002-8153-3209>;  
Andrei Manolescu - <https://orcid.org/0000-0002-0713-4664>; Halldór Guðfinnur Svavarsson - <https://orcid.org/0000-0002-1729-4098>

# **Fabrication and characterization of $\text{Si}_{1-x}\text{Ge}_x$ nanocrystals in as-grown and annealed structures: A comparative study**

M.T. Sultan<sup>1\*</sup>, V. S. Teodorescu<sup>2</sup>, J. T. Gudmundsson<sup>3, 4</sup>, A. Manolescu<sup>1</sup>, M. L. Ciurea<sup>2, 5</sup>,  
H. G. Svavarsson<sup>1\*</sup>

1. Reykjavik University, School of Science and Engineering, IS-101 Reykjavik, Iceland
2. National Institute of Materials Physics, 077125 Magurele, Romania
3. Science Institute, University of Iceland, Dunhaga 3, IS-107 Reykjavik, Iceland
4. Department of Space and Plasma Physics, School of Electrical Engineering and Computer Science, KTH Royal Institute of Technology, SE-100 44, Stockholm, Sweden
5. Academy of Romanian Scientists, 050094 Bucharest, Romania

## **AUTHOR INFORMATION**

### **\*Corresponding Author**

Halldór Guðfínnur Svavarsson

\*E-mail: [halldorsv@ru.is](mailto:halldorsv@ru.is)

Muhammad. Taha Sultan

\*E-mail: [muhammad16@ru.is](mailto:muhammad16@ru.is)

## **Abstract**

Multilayer structure comprising of SiO<sub>2</sub>/SiGe/SiO<sub>2</sub> were obtained by depositing SiO<sub>2</sub> layers using reactive direct current magnetron sputtering (dcMS), whereas, Si and Ge were co-sputtered using dcMS and high impulse power magnetron sputtering (HiPIMS), respectively. The as-grown structures subsequently underwent rapid thermal annealing (550 – 900 °C for 1 min) in N<sub>2</sub> ambient atmosphere. The structures were investigated using X-ray diffraction, high-resolution transmission electron microscopy along with photoconductive analysis, to explore structural changes and constituent properties. It is observed that the employment of HiPIMS facilitates the formation of SiGe nano-particles (~ 2.1 ± 0.8 nm) in the as-grown structure, and that presence of such nano-particles acts as a seed for heterogeneous nucleation, which upon annealing results in formation of periodically arranged columnar self-assembly of core-shell SiGe nanocrystals. Consequently an increase in photocurrent intensity by more than an order of magnitude was achieved by the annealing. Furthermore, a detailed discussion is provided on strain development within the structures, the consequent interface characteristics and its effect on the photocurrent spectra.

## **Keywords**

SiGe; SiO<sub>2</sub>; nanoparticles; TEM; photo-spectra, magnetron sputtering; HiPIMS

## Introduction

Currently, a considerable interest is being devoted to the growth of self-assembled quantum dots due to its quantum confinement effect and its numerous application in optoelectronics and nano-based structures. Semiconducting Si, Ge and SiGe nanocrystals (NCs), embedded in a dielectric oxide matrix have for instance been found to exhibit strong quantum confinement. These NCs present unique and interesting size-dependent physical properties for a wide range of application including lighting, in non-volatile memories, electronic and photovoltaic applications<sup>1,2,3</sup>. SiGe nano-based structures provide stronger quantum confinement effect than Si nanocrystals<sup>4</sup> and have the advantage of fine tunability of energy-band structure via varying the Ge atomic fraction<sup>5,6</sup>. Such properties are useful for optoelectronic devices employed for the visible to far-infrared regime<sup>4,7</sup>.

Issues commonly observed with fabrication of such structures include inhomogeneity at the matrix/nanoparticle interfaces. Several studies have been devoted to the morphology of the interface between oxide matrices and nanocrystals<sup>8,9,10</sup>. The interface of such structure has been a matter of concern in studying optical response as it may give rise to dangling bonds acting as electrically active interface traps (known as P<sub>b</sub>-type defects). These interface traps produce scattering centers, which can affect the mobility of charge carriers, thus altering the transport properties<sup>11</sup>. Moreover, sharp interfaces with an abrupt change in the dielectric constant or thermal expansion coefficients, gives rise to surface polarization effect due to the local field built up (which

assumes a crucial role for systems characterized by strong charge inhomogeneity) or strain development in the structure (influencing the size and shape of the NCs, thus resulting in alteration of the bandgap energy).

A common method to obtain NCs embedded in an oxide matrix is by thermal anneal treatment of multilayer structures. Several oxide matrices have been studied already<sup>12,13,14,15,16,17,18</sup>, of which SiO<sub>2</sub> is the most studied as it remains amorphous up to high temperatures and due to its compatibility with Si-based technology<sup>19,20,21</sup>. Various fabrication methods have been utilized to fabricate structures with embedded SiGe NCs in an oxide matrix<sup>13,17,22,23</sup>. Magnetron sputtering is one of the most versatile method and it allows for a good control of the NCs formation<sup>24</sup> by a complementary addition of rapid thermal annealing. A rather recent variation of the magnetron sputtering technique, so-called high power impulse magnetron sputtering (HiPIMS), provides an alternative approach. It is an ionized physical vapor deposition method and has shown great promise in thin film processing<sup>25,26</sup>. HiPIMS operates by pulsing the target with short unipolar voltage pulses at low frequency and short duty cycle, achieving high discharge current densities leading to a high ionization fraction of the sputtered material<sup>27,28</sup>. This approach gives denser films<sup>29</sup> and of higher crystallinity<sup>30</sup> than conventional direct current magnetron sputtering (dcMS) deposition technique.

Thermal treatment, being one of the most common method to obtain NCs embedded in an oxide matrix, improves the efficiency and stability of the devices by altering the size of the embedded NCs<sup>31,32</sup>. In the present study, a short (1 min) exposure to rapid thermal annealing is carried out over earlier investigated structures<sup>22</sup>, where the use of HiPIMS to obtain Si<sub>1-x</sub>Ge<sub>x</sub> nanoparticles in as-grown samples is demonstrated.

Upon rapid thermal annealing, periodically arranged columnar self-assembled SiGe NCs are obtained. The NCs are characterized using grazing incidence X-ray diffraction and transmission electron microscopy. The role of different character of strain relaxation and its consequent effect over NCs formation and resulting interface integrity was studied and compared with structures having thicker (~200 nm) SiGe layer<sup>23</sup>, deposited by radio-frequency magnetron sputtering (rfMS). In another previous study<sup>22</sup> we demonstrated NCs in as-grown structures with broader spectral response and improved efficiency after exposure to hydrogen plasma. The effect of annealing of such structures is yet to be explored, so as to make such structures available for devices which require controlled thermal treatments to preserve the functionality of devices<sup>32</sup>. A comparison is made to present the effect of SiGe thickness over strain accumulation in NCs (which have a deliberate effect over the size and formation of NCs, and eventually influences the photocurrent spectra), and demonstrate the effectiveness of mild thermal exposure, applicable to structures prone to decomposition at elevated temperature.

## Results and Discussion

The structures deposited in present study are similar to structures studied in our recent work<sup>22</sup> as regard the stacking order (i.e. SiO<sub>2</sub>/SiGe/SiO<sub>2</sub>) and the individual layer thicknesses. The difference in the fabrication is that for co-sputtering of SiGe layer, here we apply lower cathode voltage for the Ge deposition, i.e. 445 V instead of 470 V, at repetition frequency of 300 Hz, with an average power of 103 W. For Si (co-deposited via dcMS) the power is kept constant at 180 W.

## Structural analysis

Earlier we demonstrated that for structures with pure Ge-film sandwiched between SiO<sub>2</sub> layers, the Ge film were crystalline when sputtered by the HiPIMS method due to its high electron density in the plasma (high power density). The higher electron density increases the ionization of Ge sputtered off the target, leading to better quality film through ion bombardment. As described later in the experimental section and also in our earlier study<sup>22</sup>, the Si<sub>1-x</sub>Ge<sub>x</sub> layer was co-deposited via combined dcMS and HiPIMS from Si and Ge targets, respectively. Fig. 1(a) shows the GiXRD diffractograms for the as-grown and annealed MLs (550 - 900 °C). Two broad bands are seen for the as-grown structure. The first one corresponds to crystallographic plane (111) and the second one to the (220) and (311) planes overlapping indicating the presence of (nano) crystallites<sup>22</sup>. In Fig. 1(b), a deconvolution of the as-grown MLs was made by subtracting the background using Origin software (10.0) (counter checked using X'Pert HighScore Plus software from PANalytical, ver. 2.2). The size of the crystallites was calculated from the peak representing (111) crystallographic plane using Scherrer equation<sup>33</sup> [34] with shape (k)-factor being 0.9 and instrumental error i.e. beam broadening of 0.12. Although this is an indecisive approach<sup>22,23</sup>, the parameters used to calculate the crystallites size are mentioned in Fig. 1(b) and it was found to be  $2.1 \pm 0.8$  nm. This reduction in crystallite size, compared to previously investigated structures is due to variation in deposition parameters such as cathode voltage.

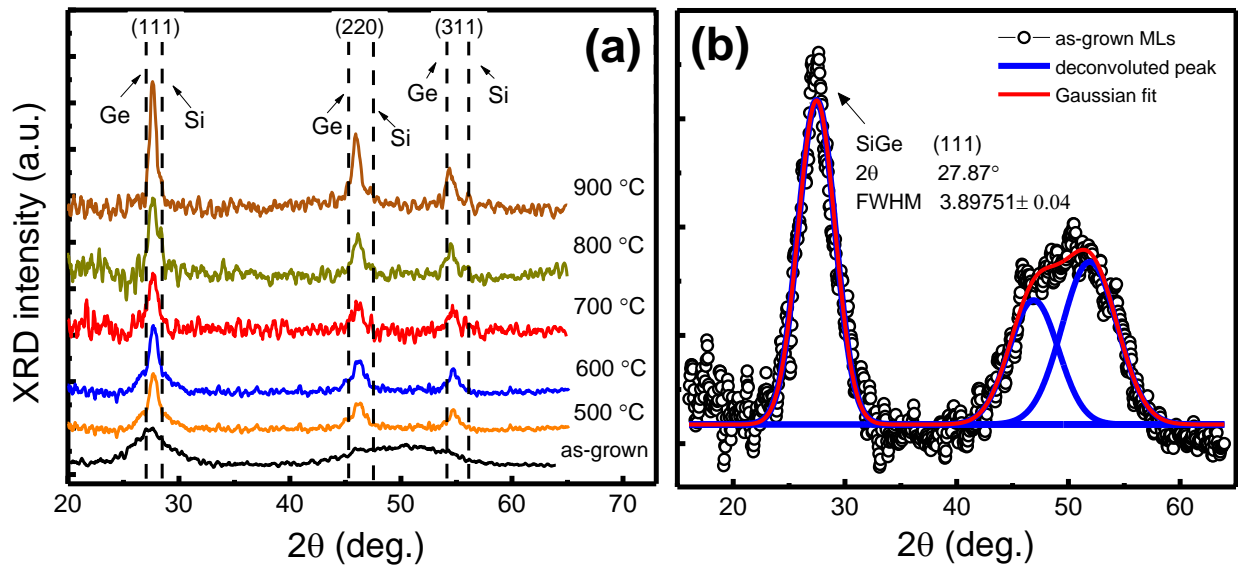


**Figure 1.** (a) GiXRD diffractogram of MLs annealed from 550 – 900 °C along with the as-grown MLs. The SiGe crystallographic peaks (111), (220) and (311) are positioned between Si and Ge tabulated ones presented by the dotted lines (for cubic Ge ( $2\theta = 27.45^\circ; 45.59^\circ; 54.04^\circ$  - ASTM 01-079-0001) and cubic Si ( $28.45^\circ; 47.31^\circ; 56.13^\circ$  - ASTM 01-070-5680)). (b) Deconvoluted GiXRD diffractogram for SiO<sub>2</sub>/SiGe/SiO<sub>2</sub> MLs, as-deposited (black circles) where, the Gaussian fit is shown by red line while deconvoluted peaks are shown in blue.

After annealing, three separate and distinctive peaks are seen (Fig. 1(a)). An increase in the XRD peak intensity was observed along with a decrease in FWHM, indicating increased crystallinity obtained via increasing anneal temperature. The size of the nanoparticles was estimated, using the crystallographic peak (111) via Scherrer equation, to vary from 7.32 to  $13.4 \pm 0.8$  nm, for annealing temperature ranging from 550 to 900 °C.. For this purpose, a more precise run was made with smaller step size and

larger time per step, which then was processed by Origin 10.0 software using multiple peak feature (not shown here). To summarize, the nanoparticles size is roughly 2 nm in the as-grown structure and increases to 7.3 – 13.4 nm upon annealing.

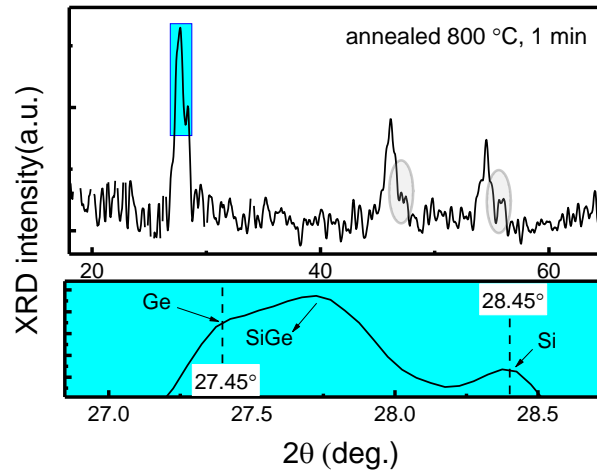


**Figure 2.** GiXRD diffractogram (upper part) with zoomed-in view (lower part) of crystallographic plane (111) of MLs annealed at 800 °C for 1 min.

Another feature to be observed here is that, for samples annealed at 550 and 600 °C (Fig. 1(a)), a sharp peak over a broad hump (extending from 25 to 31 degrees) is seen, indicating that the SiGe layer is mainly amorphous but with crystalline regions (nanoparticles) (as seen in TEM images later in Fig. 5(b) and (c)). With increased annealing temperature, peaks corresponding to the (111), (220) and (311) planes get sharper and narrower as a sign of increased crystallinity of the SiGe layer. Moreover, a small peak positioned at Si standard tabulated positions (28.45°) is observed at annealing temperatures above 600 °C (Fig. 2, selected zoomed view of peak (111) for MLs annealed at 800 °C), along with a shoulder positioned at Ge standard position (27.45°). Based on these observations, it can be concluded that the structure consists of core-shell like

nanoparticles with the core being Ge-rich  $\text{Si}_{1-x}\text{Ge}_x$  nanoparticles (crystallographic peak (111) position, shifts from  $27.87^\circ$  to  $27.754^\circ$  for MLs in as-grown and annealed at  $800^\circ\text{C}$  states, respectively) surrounded by a crystalline Si-shell with the rest being amorphous SiGeO. This behavior can be explained by phase separation in the SiGe nanoparticles due to Ge segregation<sup>34,35</sup> at higher temperature (i.e. Ge rich SiGe core) leaving a crystalline Si shell. A similar GiXRD diffractogram was observed by Tuğay et al.<sup>6</sup>, for a comparable structure composed of SiGe nanocrystals embedded in  $\text{SiO}_2$  matrix fabricated via magnetron sputtering and thermally annealed. A TEM analysis, discussed later in this section, will further elaborate on the observed nanostructure.

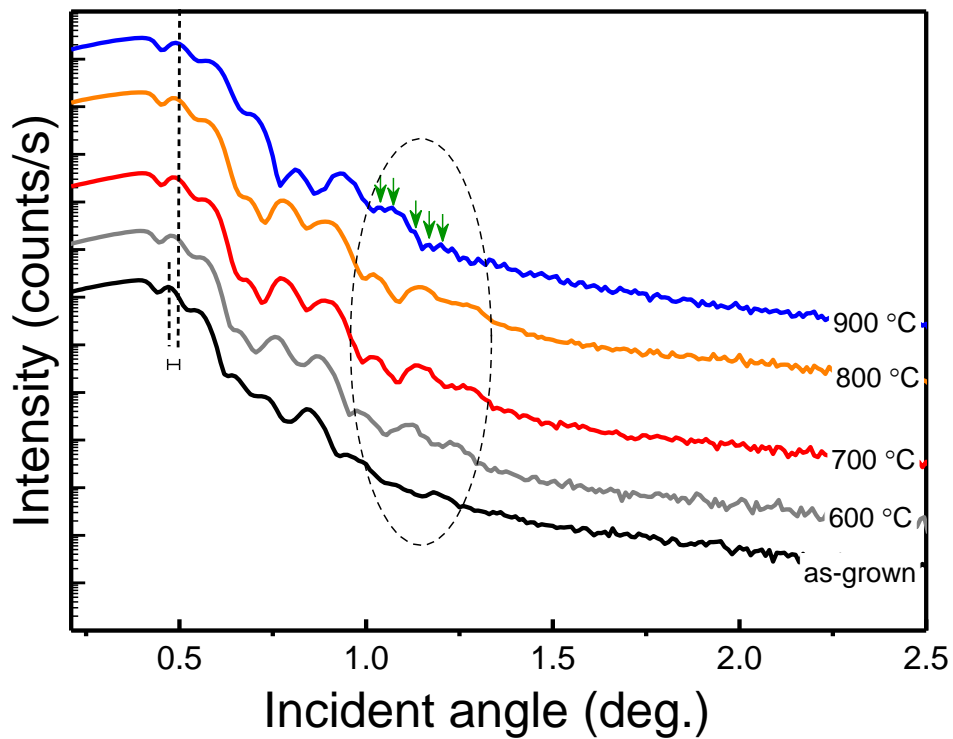


**Figure 3.** XRR plot for as-deposited and annealed (for 1 min) structures. The vertical dashed lines shows the difference in incident angle, whereas, the labeling next to each curve represents the annealing temperature.

Fig. 3 shows the X-ray reflectometry (XRR) plot of as-deposited and annealed MLs. An increase in the mass density of SiGe (3.55 to 4.17 gm/cm<sup>3</sup>) with increased annealing temperature was perceived, represented by the vertical dashed lines. In addition, a decrease in the SiGe thickness (19.57 to 17.8 nm ( $\pm 3\%$  error)) and the interface roughness (3.56 to 3.28 nm) was observed with increased annealing temperature from room temperature (as-grown) to 900 °C. All the parameters were determined by fitting the data using the X'Pert Reflectivity software. A clear evolution of fringes can be seen (shown in an enclosed area by dashed line in Fig. 3) for annealing temperature up to 700 °C, which then starts to coalesce at 800 °C and later showed appearance of Kiessig fringes (green arrows) due to scattering from the film surface and internal interfaces, thus demonstrating the alteration in the internal interface morphology. This can be further explained by the observed reduction in thickness when annealed at 800 - 900 °C and might be due to out-diffusion of Si forming Si-shell (as also explained earlier, where the crystallographic peak (111) shifts towards standard Ge position) or SiO<sub>x</sub> (will be discussed later in this section). Hence, with increased annealing temperature, formation of additional interfaces is likely to occur.

In Fig. 4(a), XTEM cross sectional image of a sample annealed at 600 °C for 1 min is presented. A total thickness of the bottom SiO<sub>2</sub> buffer layer and the top layer is about 250 nm and 40 nm respectively while the SiGe layer is 20 nm thick. Fig. 4(b) present selected area electron diffraction (SAED). The area used for electron diffraction was selected in order to have the Si substrate spots together with the ring spots of the SiGe polycrystalline layer. A description of such analysis is given in our previous work<sup>23</sup>. The Si substrate has <110> orientation. Bright spots seen are due to the Si substrate and the

smaller and less bright spots are due to SiGe nano-crystallites. The white hollow circular cloud arrives from the amorphous SiO<sub>2</sub> layers. Using the distance between the spots measured in the reciprocal space, the SiGe lattice constant can be determined in respect to the Si lattice constant. Our measurements have an estimated error of 0.5% and the results are in good agreement with the XDR measurements which corresponds to 30:70 composition for Si:Ge<sup>36</sup> (i.e. 0.599 nm is the lattice constant measured by XRD calculated via (220) crystallographic plane).

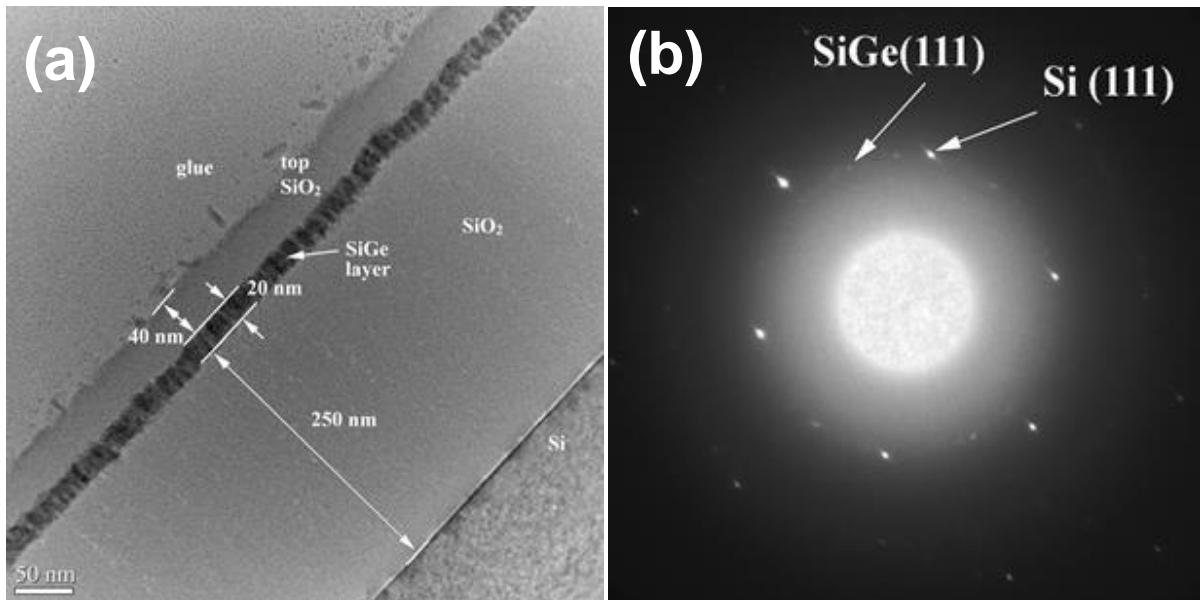


**Figure 4.** XTEM images of (a) MLs with 20 nm SiGe layer after 600 °C annealing for 1 min, (b) selected area electron diffraction over annealed MLs (600 °C, 1 min).

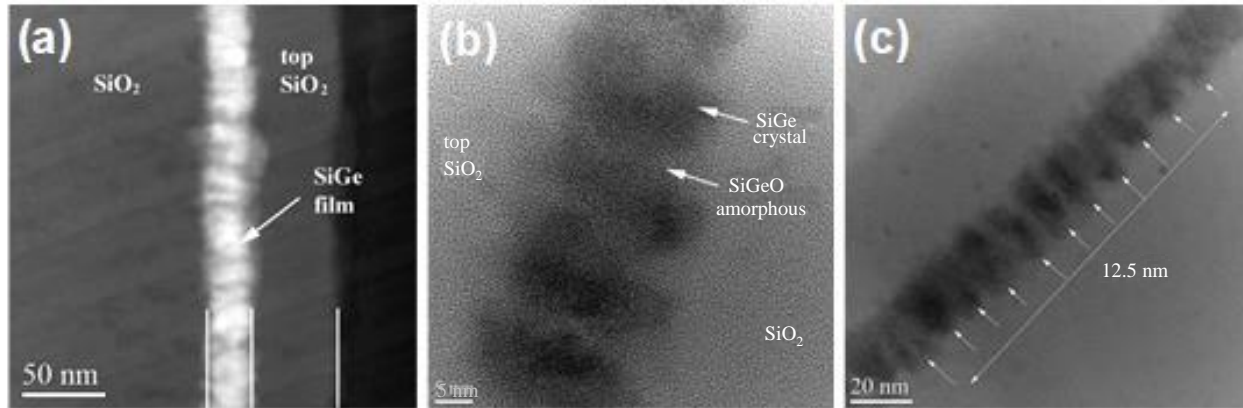


**Figure 5.** Cross-sectional (a) STEM imaging and (b, c) XTEM images of MLs annealed at 600 °C (1 min) showing columnar morphology of SiGe crystallites covered with a shell structure of amorphous SiGeO layer of ~2 nm. The crystallites have a periodicity of ~12.5 nm.

The color contrast seen in STEM image (Fig. 5(a)) emphasizes the Ge atoms density, revealing the morphology of the SiGe crystallites. It shows that the HiPIMS deposition, as explained earlier, results in high density of Ge in the SiGe layer. The SiGe nano-crystallites are columnar (ellipsoidal) oriented with the large axis parallel with the film's normal (Figs. 5(b and (c)). It is clear that the thin film (20 nm) appear stress free. The formation or modification of the planar morphology of the 20 nm SiGe layer is expected to be due to accumulation of strain field exerted by the SiO<sub>2</sub> matrix, which has been relaxed by forming corrugated edges of the SiGe film (Fig. 4(a) and 5). In contrast, for the thicker SiGe films, the strain is (partially) relaxed by forming planar defects as we demonstrated elsewhere<sup>23</sup> and discuss further below. Periodic SiGe crystallites with a ~12.5 nm period covered with amorphous SiGeO oxide (with higher portion of Si atoms than Ge atoms) are apparent in Figs. 4 and 5. The size of 12.5 nm correspond in fact to

the diameter of the SiGe ellipsoid plus the thickness of the SiGeO oxide cover-layer *i.e.* each SiGe crystallite is covered by a 2 -3 nm of SiGeO oxide, looking like a core-shell particle.

We note that the small SiGe nano-crystallites present in as-deposited MLs may have acted as a seed/nuclei for the directional crystallization of the nanoparticles as has also been suggested by Bertan et al.<sup>37</sup>. It is postulated there, that the nanosized ordered domains of Si have acted as seed crystals, resulting in a swift growth of crystals upon annealing as compared to structures without initially present nuclei. This indicates that a similar behavior may have caused such a columnar self-assembly of nanoparticles in our structures, as depicted in Figs. 4 and 5. Thus, we can anticipate heterogeneous nucleation to be a dominant process during such crystallization rather than conventional homogenous nucleation. This can be due to a better wetting of SiGe layer, which in turn reduces the free energy of change and reduces the nucleation barrier. It can also be argued that since heterogeneous nucleation occurs at preferential sites (as in our case), small nano-crystallites in as-grown MLs or even the crystallites which are under strain<sup>38,39,40,41</sup>, will further reduce the surface energy and facilitate nucleation.

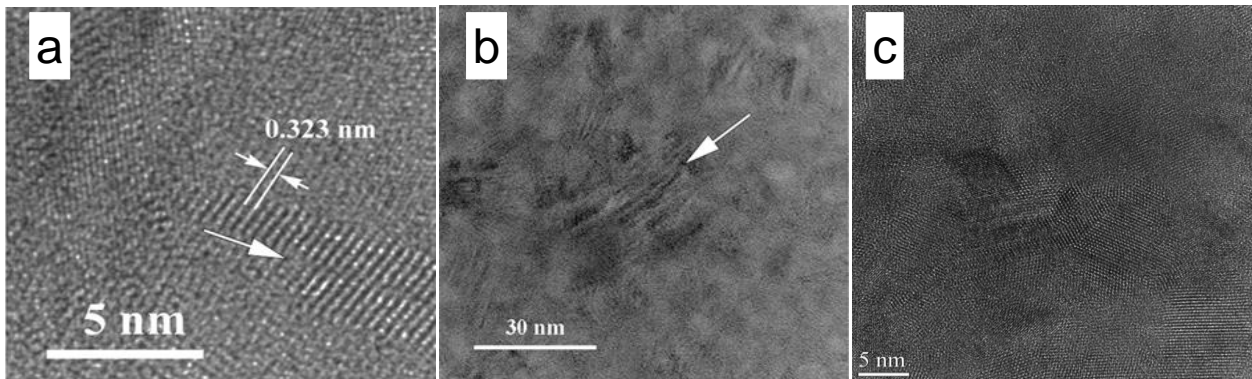


**Figure 6.**(a) TEM low-magnification image showing the contrast due to the shearing defects appearing in the SiGe crystallites, of a sample annealed at 600 °C for 1 min. (b) HRTEM image showing the lens-like shape of SiGe crystallites as a result of of shearing defects. The arrows indicate the shearing planes. (c) Sequence of microtwin bands, observed in a very thin area of the XTEM specimen (MLs with 200 nm thick SiGe<sup>23</sup>), where the SiGe NCs are not superposed in the specimen thickness. The micrographs in this figure corresponds to structure in study<sup>23</sup>.

In order to demonstrate the effect of the SiGe layer thickness on the relaxation processes Fig. 6, depicts micrographs of the previously studied structures<sup>23</sup>, where the thickness of the SiGe films was approximately 200 nm. The nanoparticles in the thicker films takes the form of lens-like morphology (Fig. 6(a)), due to the creation of shearing lattice defects (Fig. 6(b)) inside the nanocrystals, which then partially relax the stress field. These planar sharing defects are more complex than the stacking faults and the microtwins observed<sup>42</sup> in a very thin area of the structure (Fig. 6(c)). In the rest of the specimen area, the shearing defects are superposed and more complicated, as detailed in our previous study<sup>23</sup>. These defects appear only in relatively thick SiGe films in MLs as the only relaxation process-taking place. In the thin SiGe films explored here (~ 20 nm, comparable with the SiGe NCs size); these defects do not appear because other relaxation processes takes place as shown earlier. Since these shearing defects are near or in the (111) packing planes of the SiGe structure, the NC-size along the direction that is parallel to the defect plane remains large and the two others (related also to the {111} family of planes) are reduced in size, as emphasized in the TEM images in Fig. 6. A detailed microstructural TEM analysis over a relatively similar structure has been made

by Zhang et al.<sup>42</sup>. Their analysis revealed that the defects in NCs and twinning in structures were mainly related to coalescence of small nanoparticles when the structure underwent annealing whose prevalence increases with increased annealing temperature along with an increase in NCs size. A part of the stress in the structure is relieved by the formation of dislocations and the remaining stress is accommodated as local stress at the NC/matrix interface.

## Photocurrent measurements

The photocurrent spectra of as-grown structure (SiGe via dcMS and HiPIMS) is shown in Fig. 7(a). Deconvolution was carried out to obtain the individual peaks. The observed peaks were assigned to be due to interface related localized states (peak I), nanoparticles (peak N) and to capacitive coupling from Si substrate i.e. surface photovoltage (SPV) and gating effect (peak S). Fig. 7(b) shows the photocurrent for structures of the same batch that underwent annealing procedure for a short period of 1 min at different temperatures. A large increase in intensity was observed by increased annealing temperature; over ~1.2-orders of magnitude higher intensity was obtained upon annealing at 900 °C (Fig. 7(c), right y-axis), compared to as-grown structure. In this context, it is worth mentioning that samples with SiGe deposited via dcMS alone resulted in amorphous structure<sup>22</sup> which did not show any measureable photoresponse.

To demonstrate clearly the shift in peak positions and the variation in the relative peak intensities, all the spectra Fig. 7(b) were normalized to unity. One can see that with increased annealing temperature, the relative intensity of peak I increases with respect to peak N (also shown in Fig. 7(c) (left y-axis) where the ratio of the peak intensities I/N is

plotted). This modification in spectral feature can be explained based on previous work by Qin and Li<sup>43</sup> who studied interface morphology and related dangling bond effects due to annealing. In light of their results it has been postulated that there is a critical NCs size above which the interface effect prevails and below which the photoresponse is associated with quantum confinement. That is, size and surface chemistry of the NCs and oxygen-related bonds are the factors determining the photocurrent spectra. It is well understood that annealing results in the formation of dangling bonds in the structures either at the interface of the nanocrystals or in the surrounding matrix results in alteration of interface quality<sup>44,45,46</sup>. It is also thought that in the case of increased annealing temperature, a formation of Si = O bonds, along with an increase in number of dangling bonds may be possible. Increased number of dangling bonds increases the number of localized states in the band-structure along with an increase in non-radiative centers ( $P_b$ )<sup>47,48</sup>. This results in energy-width broadening of localized states with annealing temperature, resulting in bandgap alteration (Fig. 7(d) shows that both peak I and peak N blue shifts with increasing annealing temperature). These dangling bonds also act as electrically active recombination centers, which results in increased photo-response from peak I, hence an increased relative intensity with respect to peak N, as graphically expressed in Fig. 7(c).

For interface quality, it has been theoretically shown<sup>49</sup> that Si-O-Si bonds are formed at the surface when a Si-nanoparticle is oxidized<sup>50</sup>. It is likely that these relatively weak Si-O-Si and Si-Si bonds will break due to stress at the NCs/oxide-matrix interface. Thus, distorted bonds will either result in dangling bonds or eventually form a Si = O bridge since it does not require large additional amount of energy or deformation to form<sup>51,52</sup>. These

dangling bonds which act as electrically active recombination centers for charge carriers and can alter the optical properties of the structure, by contributing to oxide positive charges (depending on the location of the bond) and interface states<sup>44</sup>.

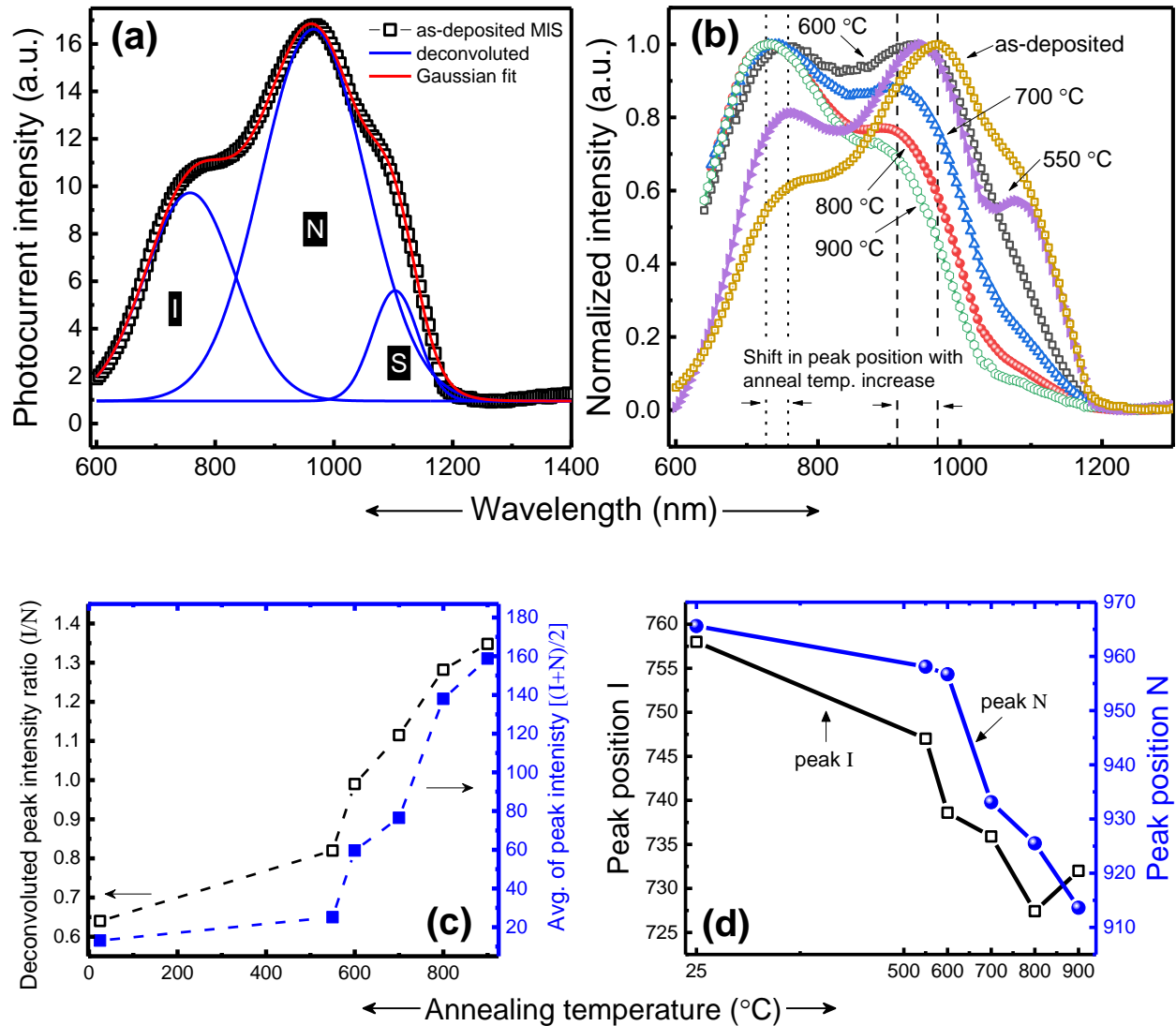


**Figure 7.** (a) Deconvoluted (Gaussian fit) room temperature photocurrent spectra of as-grown MLs. (b) Normalized photocurrent spectra of annealed (550 – 900 °C) and as-grown MLs (dotted line in the plot represents a blue-shift in peak position with increased annealing temperature). (c) Double y-axis plot, with left y-axis for alteration in intensity of

peak I with respect to peak N (i.e. peak I/N) and right y-axis showing an increase in spectral intensity as an average of peaks  $[(I+N)/2]$ , as a function of annealing temperature. (d) Peak positions of curves I and N versus temperature for fixed annealing time of 1 min (values obtained by deconvoluting the spectra).

In addition, the annealing of the structure results in reconstruction/ordering of the matrix structure<sup>53</sup>, which consequently govern the strain induced over the NCs, and can affect the NCs crystallinity<sup>39,40</sup>. The degree of matrix ordering determines the accommodation of the growing crystallites i.e. the matrix will resist the NCs to expand freely. Thus, as a result of growing crystallites, strain is introduced at the interface between the matrix and NCs<sup>38,39,54</sup>, which in turn alters the bandgap (Fig. 7(d)). Additionally, the role of thermal expansion coefficient of SiGe/ SiO<sub>2</sub> and lattice mismatch between Si and Ge (4.2 %<sup>55,31</sup>), that assists in the development of strain in structure, should be taken into account<sup>38</sup>. From the above discussion, it can be summarized that the annealing temperature does affect the structuring of the oxide matrix which in turn induces strain in the structure and therefore alters the interface morphology, hence inducing a change in the intensity ratio of peak I/N (Fig. 7(d)).

## Conclusion

SiGe nanocrystals sandwiched between SiO<sub>2</sub> layers were fabricated by co-sputtering using HiPIMS and dcMS followed by rapid thermal annealing (1 min) at various temperatures. It is shown that application of HiPIMS deposition facilitates the formation of small nanoparticles/clusters in the as-grown structures. A suitable selection of annealing temperature and time results in the formation of columnar (core-shell structure) self-

assembly of SiGe nanoparticles, as comprehensively studied by GiXRD and TEM analysis. Such columnar self-assembly is attributed to stated dominant strain relaxation process, further assisted by already present small nanoparticles in the as-grown structures, acting as seed crystals for heterogeneous nucleation. The photocurrent study reveals that the presence of structural strain and resulting NCs/matrix interface morphology plays a vital role in determining the spectral feature and sensitivity.

## **Experimental apparatus and method**

Multilayer structure with stacking order of SiO<sub>2</sub>/SiGe/SiO<sub>2</sub> was prepared by magnetron sputtering over a 12×12 mm<sup>2</sup> Si (001) substrates. Prior to deposition, the substrate was etched with 2M hydrofluoric acid (HF) for 120 s to remove native oxide. For the SiGe films, co-sputtering was carried out from individual targets of (6N purity) Si and Ge, respectively. Deposition of Si was carried out via dcMS at 180 W, whereas Ge was sputtered via HiPIMS operating at 445 V cathode voltage at a repetition frequency of 300 Hz. An average power of 103 W, with an average current density and peak power density of 233 mA/cm<sup>2</sup> and 107 W/cm<sup>2</sup>, respectively was maintained over the full target area. 3.0" MAK Planar Magnetron Sputter Source, MeiVac, with Nd/FeB magnets was employed. Each individual target (Si and Ge) experience different magnetic field strength |B|, stronger for the Ge target and weaker for Si (opposite to our previous study<sup>22</sup> i.e. stronger for Si and weaker for Ge). Since the deposition rate of Ge is usually higher than that of Si, the |B| is selected accordingly. It has been acknowledged for both dcMS and HiPIMS that the increase in |B| results in decreased deposition rate (DR)<sup>56,57,58</sup>, and for HiPIMS it often increased ionized flux fraction. This explanation justifies the need to reconsider the

differences in sputter parameters and deposition rates and the resulting change in crystalline size as mentioned in section 2. Additionally, a constant ratio between Si and Ge was maintained in the present study, as confirmed by GiXRD analysis.

For the SiO<sub>2</sub> layers, deposition was carried out via reactive dcMS sputtering. A detailed description of the sputter technique and equipment used, along with a schematic of as-grown structure is given elsewhere<sup>22</sup>. After deposition, the structure underwent annealing for 1 min in a rapid thermal processor (RTA, Jipelec JetFirst 200) at temperatures ranging from 550 to 900 °C, in an N<sub>2</sub> ambient atmosphere.

The structural investigation of the fabricated MLs was carried out by grazing incidence XRD (GIXRD) and X-ray reflectometry (XRR) via Philips X'pert diffractometer (CuK<sub>α</sub>, 0.15406 nm, precision of 0.00001°) and Jeol ARM 200F transmission electron microscopy (TEM). For the X-ray diffraction scans, 2×Ge (220) asymmetrical hybrid monochromator utilizing line focus, with a 1/4° divergence slit and a 0.27° parallel plate collimator was used. The measurement run was made over 0.005 °/s. scan speed.

For photoconductive measurement, Al-contacts (1×4 mm<sup>2</sup>) in co-planar geometry with a gap of 4 mm between them were deposited by evaporation. A schematic of the photocurrent setup and the procedure to acquire photo-spectra can be found elsewhere<sup>23</sup>.

## **Acknowledgements**

This work is funded through M-ERA.NET project PhotoNanoP UEFISCDI Contract no. 33/2016, PCE project UEFISCDI Contract no. 122/2017 and by Romanian Ministry of Research and Innovation through NIMP Core Program PN16-480102 and by the

Technology Development Fund of the Icelandic Centre for Research, grant no. 159006-0611.

## References

- (1) Tevaarwerk, E.; Rugheimer, P.; Castellini, O. M.; Keppel, D. G.; Utley, S. T.; Savage, D. E.; Lagally, M. G.; Eriksson, M. A. *Appl. Phys. Lett.* **2002**, *80*, 4626–4628.
- (2) Buljan, M.; Pinto, S. R. C.; Kashtiban, R. J.; Rolo, A. G.; Chahboun, A.; Bangert, U.; Levichev, S.; Holý, V.; Gomes, M. J. M. *J. Appl. Phys.* **2009**, *106*, 084319.
- (3) Mihalache, D. *J. Optoelectron. Adv. Mater* **2011**, *13*, 1055–1066.
- (4) Lepadatu, A. M.; Stavarache, I.; Maraloiu, A.; Palade, C.; Serban, T. V.; Magdalena, C. L. In Proceeding of the International Semiconductor Conference CAS (IEEE), Sinaia, Romania, October 15 - 17, 2012; pp 109–112.
- (5) Pan, S. W.; Zhou, B.; Chen, S. Y.; Li, C.; Huang, W.; Lai, H. K. *Appl. Surf. Sci.* **2011**, *258*, 30–33.
- (6) Tuğay, E.; Ilday, S.; Turan, R.; Finstad, T. G. *J. Lumin.* **2014**, *155*, 170–179.
- (7) Vieira, E. M. F.; Toudert, J.; Rolo, A. G.; Parisini, A.; Leitão, J. P.; Correia, M. R.; Franco, N.; Alves, E.; Chahboun, A.; Martín-Sánchez, J.; et al. *Nanotechnology* **2017**, *28* (34), 345701.
- (8) Kepa, J.; Stesmans, A.; Afanas'ev, V. V. *Appl. Surf. Sci.* **2014**, *291*, 20–24.

- (9) Houssa, M.; Pourtois, G.; Meuris, M.; Heyns, M. M.; Afanas'ev, V. V.; Stesmans, A. *Microelectron. Eng.* **2011**, *88*, 383–387.
- (10) Madia, O.; Nguyen, A. P. D.; Thoan, N. H.; Afanas'ev, V.; Stesmans, A.; Souriau, L.; Slotte, J.; Tuomisto, F. *Appl. Surf. Sci.* **2014**, *291*, 11–15.
- (11) Tsetseris, L.; Pantelides, S. T. *Microelectron. Eng.* **2011**, *88*, 395–398.
- (12) Lepadatu, A.-M.; Slav, A.; Palade, C.; Dascalescu, I.; Enculescu, M.; Iftimie, S.; Lazanu, S.; Teodorescu, V. S.; Ciurea, M. L.; Stoica, T. *Sci. Rep.* **2018**, *8*, 4898.
- (13) Pinto, S. R. C.; Kashtiban, R. J.; Rolo, A. G.; Buljan, M.; Chahboun, A.; Bangert, U.; Barradas, N. P.; Alves, E.; Gomes, M. J. M. *Thin Solid Films* **2010**, *518*, 2569–2572.
- (14) Stavarache, I.; Lepadatu, A.-M.; Stoica, T.; Ciurea, M. L. *Appl. Surf. Sci.* **2013**, *285*, 175–179.
- (15) Choi, W. .; Kanakaraju, S.; Shen, Z. .; Li, W. *Appl. Surf. Sci.* **1999**, *144–145*, 697–701.
- (16) Jie, Y. X.; Wu, X.; Huan, C. H. A.; Wee, A. T. S.; Guo, Y.; Zhang, T. J.; Pan, J. S.; Chai, J.; Chua, S. J. *Surf. Interface Anal.* **1999**, *28*, 195–199.
- (17) Vieira, E. M. F.; Pinto, S. R. C.; Levichev, S.; Rolo, A. G.; Chahboun, A.; Buljan, M.; Barradas, N. P.; Alves, E.; Bernstorff, S.; Conde, O.; et al. *Microelectron. Eng.* **2011**, *88*, 509–513.
- (18) Ray, S. K.; Das, S.; Singha, R. K.; Manna, S.; Dhar, A. *Nanoscale Res. Lett.* **2011**, *6* (1), 224.

- (19) Chew, H. G.; Choi, W. K.; Foo, Y. L.; Zheng, F.; Chim, W. K.; Voon, Z. J.; Seow, K. C.; Fitzgerald, E. A.; Lai, D. M. Y. *Nanotechnology* **2006**, *17*, 1964–1968.
- (20) Zschintzsch, M.; von Borany, J.; Jeutter, N. M.; Mücklich, A. *Nanotechnology* **2011**, *22* (46), 465302.
- (21) Barradas, N. P.; Alves, E.; Vieira, E. M. F.; Parisini, A.; Conde, O.; Martín-Sánchez, J.; Rolo, A. G.; Chahboun, A.; Gomes, M. J. M. *Nucl. Instruments Methods Phys. Res. Sect. B Beam Interact. with Mater. Atoms* **2014**, *331*, 89–92.
- (22) Sultan, M. T.; Gudmundsson, J. T.; Manolescu, A.; Stoica, T.; Ciurea, M. L.; Svavarsson, H. G. *Appl. Surf. Sci.* **2019**, *479*, 403–409.
- (23) Sultan, M. T.; Manolescu, A.; Gudmundsson, J. T.; Torfason, K.; Alexandru Nemnes, G.; Stavarache, I.; Logofatu, C.; Teodorescu, V. S.; Ciurea, M. L.; Svavarsson, H. G. *Appl. Surf. Sci.* **2019**, *469*, 870–878.
- (24) Palade, C.; Slav, A.; Lepadatu, A. M.; Maraloiu, A. V.; Dascalescu, I.; Iftimie, S.; Lazanu, S.; Ciurea, M. L.; Stoica, T. *Appl. Phys. Lett.* **2018**, *113*, 213106.
- (25) Helmersson, U.; Lattemann, M.; Bohlmark, J.; Ehiasarian, A. P.; Gudmundsson, J. T. *Thin Solid Films* **2006**, *513*, 1–24.
- (26) Lundin, D.; Sarakinos, K. *J. Mater. Res.* **2012**, *27*, 780–792.
- (27) Gudmundsson, J. T. *Vacuum* **2010**, *84*, 1360–1364.
- (28) Gudmundsson, J. T.; Brenning, N.; Lundin, D.; Helmersson, U. *A Vacuum, Surfaces, Film.* **2012**, *30*, 030801.

- (29) Samuelsson, M.; Lundin, D.; Jensen, J.; Raadu, M. A.; Gudmundsson, J. T.; Helmersson, U. *Surf. Coatings Technol.* **2010**, *205*, 591–596.
- (30) Alami, J.; Persson, P. O. Å.; Music, D.; Gudmundsson, J. T.; Bohlmark, J.; Helmersson, U. *J. Vac. Sci. Technol. A Vacuum, Surfaces, Film.* **2005**, *23*, 278–280.
- (31) Aqua, J. N.; Berbezier, I.; Favre, L.; Frisch, T.; Ronda, A. *Phys. Rep.* **2013**, *522*, 59–189.
- (32) Stavarache, I.; Maraloiu, V. A.; Negrița, C.; Prepelita, P.; Gruia, I.; Iordache, G. *Semicond. Sci. Technol.* **2017**, *32*, 105003.
- (33) Patterson, A. L. *Phys. Rev.* **1939**, *56*, 978–982.
- (34) Mogaddam, N. A. P.; Alagoz, A. S.; Yerci, S.; Turan, R.; Foss, S.; Finstad, T. G. *J. Appl. Phys.* **2008**, *104*, 124309.
- (35) M. L. Ciurea, A. L. *Dig. J. Nanomater. Biostructures* **2015**, *10*, 59–87.
- (36) Dismukes, J. P.; Ekstrom, L.; Paff, R. J. *J. Phys. Chem.* **1964**, *68*, 3021–3027.
- (37) Bertran, E.; Sharma, S. N.; Viera, G.; Costa, J.; St'ahel, P.; Cabarrocas, P. R. i. *J. Mater. Res.* **1998**, *13*, 2476–2479.
- (38) Bahariqushchi, R.; Raciti, R.; Kasapoğlu, A. E.; Gür, E.; Sezen, M.; Kalay, E.; Mirabella, S.; Aydinli, A. *Nanotechnology* **2018**, *29*, 185704.
- (39) Zatoryb, G.; Podhorodecki, A.; Misiewicz, J.; Cardin, J.; Gourbilleau, F. *Nanoscale Res. Lett.* **2013**, *8* (1), 40.

- (40) Liao, P. H.; Hsu, T. C.; Chen, K. H.; Cheng, T. H.; Hsu, T. M.; Wang, C. C.; George, T.; Li, P. W. *Appl. Phys. Lett.* **2014**, *105*, 172106.
- (41) Zatoryb, G.; Misiewicz, J.; Wilson, P. R. J.; Wojcik, J.; Mascher, P.; Podhorodecki, A. *Thin Solid Films* **2014**, *571*, 18–22.
- (42) Zhang, M.; Cai, R.; Zhang, Y.; Wang, C.; Wang, Y.; Ross, G. G.; Barba, D. *Mater. Charact.* **2014**, *93*, 1–9.
- (43) Qin, G. G.; Li, Y. J. *Phys. Rev. B* **2003**, *68*, 085309.
- (44) Yakimov, A. I.; Kirienko, V. V.; Armbrister, V. A.; Dvurechenskii, A. V. *Semicond. Sci. Technol.* **2014**, *29*, 085011.
- (45) Brown, W. D.; Khaliq, M. A. *Thin Solid Films* **1990**, *186*, 73–85.
- (46) Dashiell, M. W.; Denker, U.; Müller, C.; Costantini, G.; Manzano, C.; Kern, K.; Schmidt, O. G. *Appl. Phys. Lett.* **2002**, *80*, 1279–1281.
- (47) Nazarov, A. N.; Lysenko, V. S.; Nazarova, T. M. *Semicond. Physics, Quantum Electron. Optoelectron.* **2008**, *11*, 101–123.
- (48) Nikitin, T.; Khriachtchev, L. *Nanomaterials* **2015**, *5*, 614–655.
- (49) Wolkin, M. V.; Jorne, J.; Fauchet, P. M.; Allan, G.; Delerue, C. *Phys. Rev. Lett.* **1999**, *82*, 197–200.
- (50) Szekeres, A.; Alexandrova, S. *Vacuum* **1996**, *47*, 1483–1486.
- (51) Puzder, A.; Williamson, A. J.; Grossman, J. C.; Galli, G. *J. Chem. Phys.* **2002**, *117*, 6721–6729.

- (52) López, M.; Garrido, B.; García, C.; Pellegrino, P.; Pérez-Rodríguez, A.; Morante, J. R.; Bonafos, C.; Carrada, M.; Claverie, A. *Appl. Phys. Lett.* **2002**, *80*, 1637–1639.
- (53) Hadjisavvas, G.; Kelires, P. C. *Phys. Rev. Lett.* **2004**, *93*, 226104.
- (54) Hadjisavvas, G.; Remediakis, I. N.; Kelires, P. C. *Phys. Rev. B* **2006**, *74*, 165419.
- (55) Ye, H.; Yu, J. *Sci. Technol. Adv. Mater.* **2014**, *15*, 024601.
- (56) Ekpe, S. D.; Jimenez, F. J.; Field, D. J.; Davis, M. J.; Dew, S. K. *J. Vac. Sci. Technol. A Vacuum, Surfaces, Film.* **2009**, *27*, 1275–1280.
- (57) Papa, F.; Gerdes, H.; Bandorf, R.; Ehiasarian, A. P.; Kolev, I.; Braeuer, G.; Tietema, R.; Krug, T. *Thin Solid Films* 2011, *520*, 1559–1563.
- (58) Čapek, J.; Hála, M.; Zabeida, O.; Klemberg-Sapieha, J. E.; Martinu, L. *J. Phys. D. Appl. Phys.* **2013**, *46*, 205205.